RSC Advances

PAPER

View Article Online
View Journal | View Issue

Cite this: *RSC Adv.*, 2023, **13**, 25738

Synthesis of Pr^{3+}-doped WO_3 particles: correlation between photoluminescent and photocatalytic properties†

L. X. Lovisa, *[a] D. F. dos Santos,[b] A. A. G. Santiago,[b] M. D. Teodoro,[c] M. R. D. Bomio[b] and F. V. Motta[b]

The WO_3 and WO_3:Pr^{3+} particles were successfully synthesized by the co-precipitation method. The XRD analysis with Rietveld refinement revealed the formation of a monoclinic phase for WO_3 and for doped samples, this result was later confirmed by Raman spectroscopy studies. The presence of Pr^{3+} in the WO_3 crystalline lattice induced structural and optical changes in the particles, increasing the crystallite size, distorting the clusters (shortening of the W–O bonds), favoring the crystallinity and changing the optical gap. The predominant morphology of the particles of WO_3 and WO_3:Pr^{3+} obtained was nanocubes constituted by the superposition of plates of nanometric thicknesses. The photoluminescence of WO_3 and WO_3:Pr^{3+} was produced by the existence of surface defects in the particles. The increase in the concentration of Pr^{3+} promoted an increase in the intensity of PL, due to the increase in the rate of recombination of electron/hole charges. The WO_3 sample exhibited emission in the white region due to the adjustment of simultaneous electronic transitions in the blue, green and red regions, characteristic of the broadband spectrum. The interval of the 2.65 eV gap band and the high efficiency in the separation of the photogenerated charges (e^-/h^+) with the low recombination rate contributed to the photocatalytic degradation of Crystal Violet (CV) by the catalyst. The WO_3:4% Pr^{3+} sample showed the best photocatalytic efficiency, degrading 73% of the CV dye in 80 minutes. This result was associated with a reduction in particle size and density of oxygen vacancies on the material surface.

Received 31st July 2023
Accepted 23rd August 2023

DOI: 10.1039/d3ra05136f

rsc.li/rsc-advances

1. Introduction

Water reservoirs are extremely important for the maintenance of life by providing water for people's basic needs. In contrast, these same reservoirs are used as a final destination for by-products produced by the industrial sector.[1] Environmental and health problems associated with hazardous waste and toxic pollutants in water have attracted much attention.[2,3] Especially, dyes are the main residues of these effluents, these compounds being difficult to degrade and highly toxic to the environment.[4,5] In the face of this impasse, the search for practical, viable and sustainable solutions that address this issue becomes of great importance.

Advanced Oxidative Processes (POAs) have found space in the research and applications of wastewater treatment technologies due to their diversity of technologies involved and the areas of potential application. POAs address efficient methods that reduce environmental impacts. The effectiveness of POAs is based on the production of reactive free radicals ($^{\cdot}OH^-$).[6,7]

Metallic oxide semiconductor nanoparticles, as heterogeneous photocatalysts, have attracted a lot of attention due to their physical and chemical properties adjustable by size. These materials have a longer service life and are chemically stable under extreme conditions, such as high temperature or pressure.[8,9] Semiconductors have been presented as an excellent choice in the area of photocatalysis, as well as in energy storage.[10–12] What draws attention to the use of semiconductors for the photocatalytic process is its electronic structure, composed of a valence band (E_{VB}), a conduction band (E_{CB}) and a spacing between these bands called the bandgap.[13] With the irradiation of light, with energy equal to or greater than the bandgap energy of the material, electrons are transferred from the E_{VB} to the E_{CB}, generating electric pairs e^-/h^+. The generation of these electron pairs promotes the formation of reactive oxygen species (ROS) such as $^{\cdot}OH^-$ and O_2^-, which promote the degradation of organic contaminants.[14,15] However,

[a]Special Coordination of Materials Engineering, Federal University of Santa Catarina, Blumenau, Santa Catarina, Brazil. E-mail: laura.lovisa@ufsc.br

[b]Department of Materials Engineering, LSQM – Laboratory of Chemical Synthesis of Materials, Federal University of Rio Grande do Norte, P. O. Box 1524, 59078-900, Natal, RN, Brazil

[c]Department of Physics, Federal University of São Carlos, São Carlos, São Paulo, 13565-905, Brazil

† Electronic supplementary information (ESI) available. See DOI: https://doi.org/10.1039/d3ra05136f

semiconductors have some limitations such as recombination of photoelectron pairs and e^-/h^+ and a wide bandgap. These difficulties can be overcome by performing some modifications such as nanoparticles, doping, heterojunctions.[16,17]

Specifically, tungsten trioxide (WO_3) is characterized by being a type n semiconductor, with a gap energy of approximately 2.8 eV.[18–20] WO_3 has interesting properties related to applications in photocatalysis, in solar cells and energy generation due to its thermochemical stability, it has a high absorption of light.[19,21,22] Another distinguishing feature of WO_3 is that it is an environmentally friendly material, which makes it attractive for the use of complete mineralization of pollutants.[23]

This article proposes to present the characterizations and analyzes of the structural, morphological and photocatalytic properties of the WO_3 and WO_3:Pr^{3+} particles. Evaluates the effect of Pr^{3+} as doping on the studied properties.

2. Experimental

2.1 Materials

Sodium tungstate dihydrate ($Na_2WO_4 \cdot 2H_2O$), praseodymium(III) nitrate ($Pr(NO_3)_3 \cdot xH_2O$) (Alfa Aesar), nitric acid (Synth) and distilled water were used as received to prepare the WO_3 and WO_3:Pr^{3+} particles.

2.2 Precipitation synthesis of the WO_3 and WO_3:Pr^{3+} particles

All chemicals used were analytical grade. First, sodium tungstate dihydrate ($Na_2WO_4 \cdot 2H_2O$) was dissolved in nitric acid (volume ratio 1 : 1) to prepare 0.1 M solution. Pr^{3+} (($Pr(NO_3)_3 \cdot xH_2O$)) was added stoichiometrically to the reaction medium keeping the magnetic stirring and the synthesis temperature at 60 °C constant. The pH of the solution was adjusted to 1 with the addition of nitric acid. The formation of a yellow precipitate was observed. This precipitate was filtered and carefully washed three times in distilled water to completely remove impurity ions from the precipitate. After that, the precipitate was dried at 60 °C for 24 hours and subsequently calcined at 800 °C for 2 h at a heating rate of 10 °C min^{-1} to obtain WO_3 and WO_3:Pr^{3+} particles.

2.3 Characterizations

The WO_3 and WO_3:Pr^{3+} particles were structurally characterized by XRD using a Shimadzu XRD 7000 instrument with Cu-Kα radiation (λ = 1.5406 Å) in the 2θ range from 10 to 80° at a scanning rate of 0.02 s^{-1}. Raman spectroscopy spectra were measured by FT-Raman Bruker-RFS 100 using an Nd:YAG laser operating at 1064 nm with nominal power of 55 mW as the excitation source. The morphologies were investigated using a field-emission gun scanning electron microscope (FE-SEM; Carl Zeiss, Supra 35-VP Model, Germany) operated at 6 kV. The UV-vis diffuse reflectance spectrum was measured at room temperature using a Shimadzu UV-2600 spectrophotometer. Photoluminescence measurements were performed using a 355 nm excitation laser (Cobolt/Zouk) with a power of 1.3 mW. The detection system consists of a 19.3 cm spectrometer and a silicon CCD detector (Andor-Kymera/Idus).

The photocatalytic properties of the powders combined as a catalyst agent were estimated by the degradation of the Crystal Violet (CV) with a molecular formula [$C_{28}H_{31}ClN_2O_3$] (99.5% purity, Mallinckrodt), illuminated by UV lamps in aqueous solution. First, 50 mL of the CV solution (1×10^{-5} mol L^{-1} concentration) was mixed with 0.05 g of the material to be tested in a quartz beaker. This mixture was kept understirring at a controlled temperature (25 °C) and lit by six UVC lamps (15 W TUV Philips, with a maximum intensity of 254 nm = 4.9 eV). The sample was kept under stirring for 30 min with the lights off to disregard possible adsorption events. An aliquot of the samples was taken at each 10 minute time interval and centrifuged at 9000 rpm for 5 minutes to remove the suspended particles. Finally, the variations in the maximum absorption band of each aliquot were measured by UV-Vis absorbance with spectral measurements using a Shimadzu UV-2600 spectrophotometer with a wavelength in the range of 400 to 800 nm.

3. Results and discussion

3.1. X-ray diffraction

Fig. 1 shows the XRD patterns of the particles of pure WO_3 and WO_3:x% Pr^{3+} (x% = 1, 2 and 4%). The changes identified in the results were attributed to the structural distortions imposed by the presence of Pr^{3+} in the WO_3 lattice. All the diffraction peaks of the WO_3:Pr^{3+} samples are indexed to the WO_3 monoclinic phase structure (γ-WO_3) with the lattice parameters of a = 7.3088 Å, b = 7.5345 Å, c = 7.6957 Å and β = 90.918° (JCPDS card no. 43-1035).[24] Highlighted in Fig. 1 shows the planes ($\bar{1}32$), (123), ($3\bar{1}2$), (312) of lesser intensity located around 2θ = 45° referring to the monoclinic phase.

It is observed that there are no secondary phases, showing that the replacement of the W^{6+} ions by the Pr^{3+} ions occurred successfully. It is observed that the diffraction peaks (002), (020), (200) show a small change of position for the region of greater angle with the increase of the concentration of Pr^{3+}. These variations are associated with changes in lattice parameters due to the difference between the ionic radius of W^{6+} = (0.6 Å) and Pr^{3+} (1.12 Å).[25,26] The intensity of the diffraction peaks of these planes increases significantly with the increase of the Pr^{3+} concentration, indicating that the Pr^{3+} dopant favors the crystallinity of the material.[27] According to Upadhyay *et al.*,[28] the improvement in crystallinity may be related to the incorporation of the dopant in the WO_3 lattice, which reduces the density of the nucleation centers, which, in turn, favors the growth of the crystal grains. The size of the crystallite was estimated by the Scherrer equation.[29]

The Rietveld refinements of the samples were performed using XRD data using the General Structure Analysis System (GSAS) program with the EXPGUI graphical interface was used to perform the refinements. The refinements were performed with the spatial group $P2_1/n$ within the range of 2θ from 10°–80°. Fig. 2 shows the refined XRD standard for the WO_3 and WO_3:Pr^{3+} samples. The lattice parameters (a, b, c and β), the values of the quality coefficients of the refinement (X^2, W_{rp}, W_p,

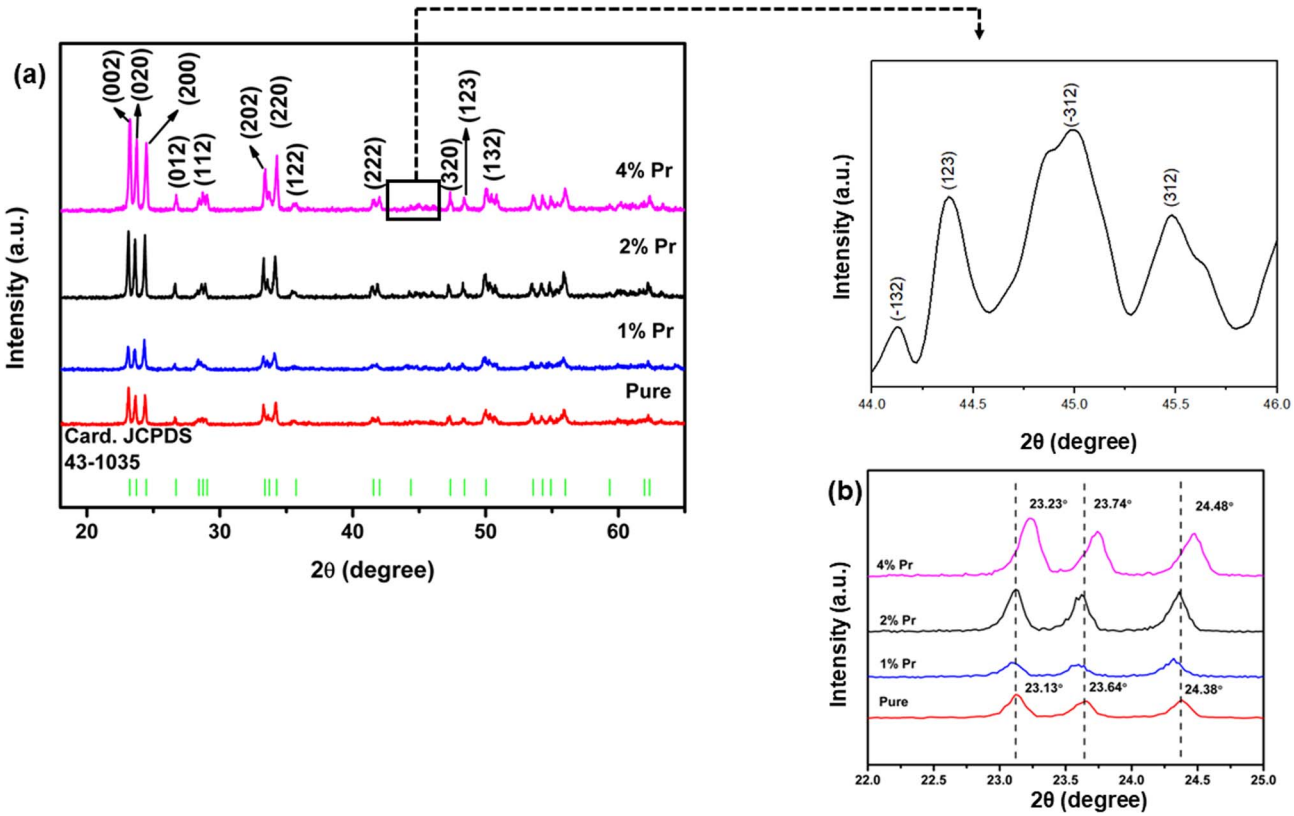

Fig. 1 XRD pattern of samples WO_3:Pr^{3+}; representation of the γ-WO_3 unit cell.

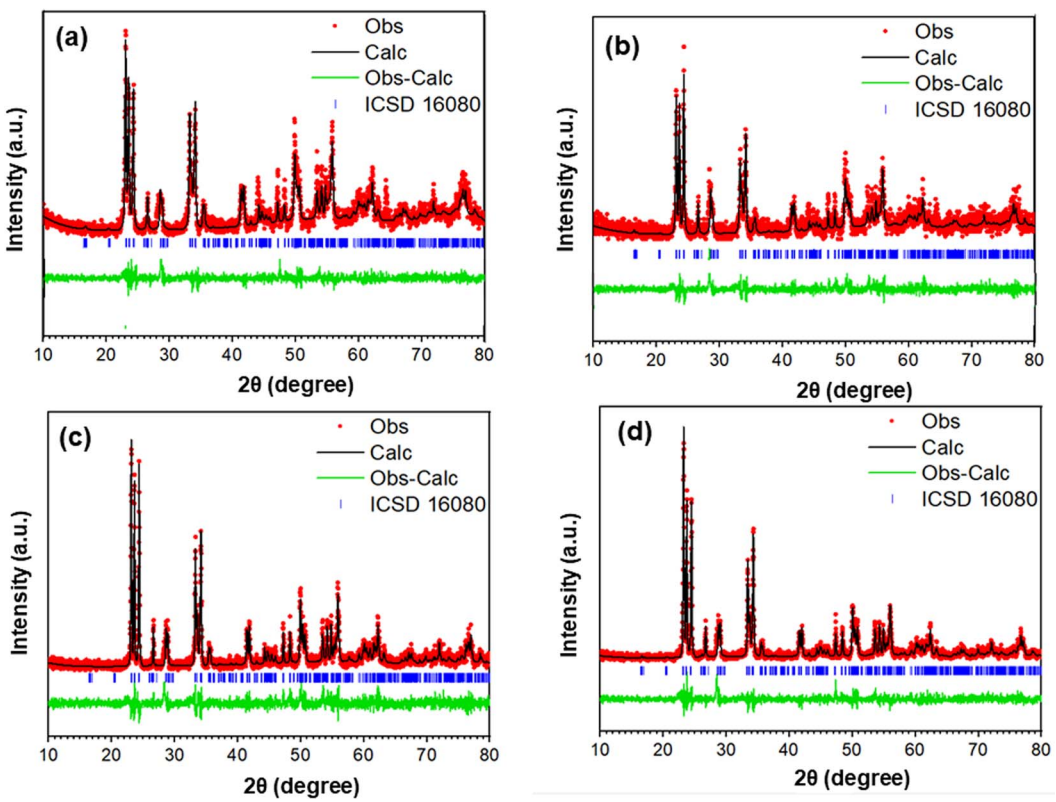

Fig. 2 Representation of the WO_3 and WO_3:Pr^{3+} refinements.

R_f^2) and the size of the crystallite (D) are recorded in Table S1 of ESI.† The quality coefficient values of the refinement are within the acceptable values as a good fit between the observed data and the calculated data.

Based on calculations of functional density theory (DFT), several studies[30–33] show that the electronic structure of the different phases of WO_3 is related to variations in the length of W–O bonds along the directions in the crystal with orbital anti-bond interactions – resulting connections, which give rise to the hybridized orbitals W(5d) and O(2p) in the conduction band and valence band states, respectively. The properties relevant to each phase of WO_3 are attributed to the distortions present in the octahedral clusters.[31,34] We observe a shortening of the W–O bonds from the introduction of Pr^{3+} to replace the W atoms in WO_3 due to the difference in the size of the ionic radius of the cátions, generating distortions of the WO_3 lattice. The lengths of the W–O connections are recorded in Table S2.†

3.2 Raman spectroscopy

To better understand the chemical structure and chemical bonds present in WO_3:Pr^{3+} samples, Raman spectra were performed in the range of 100 to 1000 cm^{-1}. Fig. 3 shows the Raman spectra, the presence of 5 characteristic bands of the γ-WO_3 phase is observed. This result confirms what was presented in the XRD discussion. It is possible to identify bands at 270 and 325 cm^{-1} that correspond to the flexion vibration modes of the δ(O–W–O) connections.[35,36] The characteristic bands at 712 and 801 cm^{-1} are characteristics of WO_3 of the monoclinic phase and associated with the ν(W–O–W) connections lengthening mode.[35,37] Vibrational modes at low frequencies, as you can see at 129 cm^{-1}, are associated with lattice modes. Chen *et al.*[38] attributed the widening of the WO_3 Raman bands to the heat treatment effect that suggested small changes in their structure. According to the authors, oxygen vacancies were introduced in γ-WO_3 crystals causing an increase in the W–O bond in the Raman spectrum, indicating that the structure of WO_3 was altered by the formation of these defects as a result of annealing.

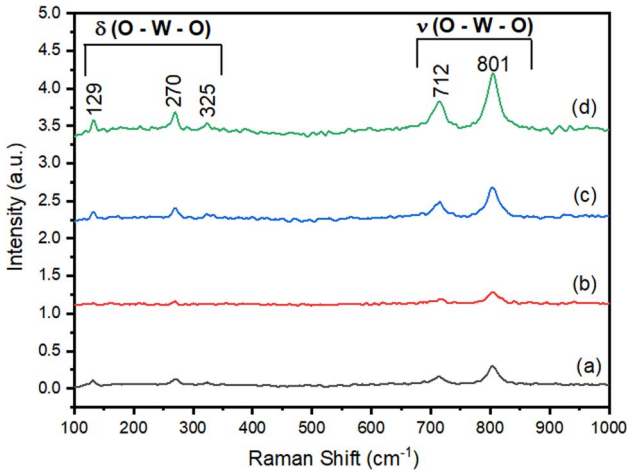

Fig. 3 Raman spectroscopy of samples WO_3:Pr^{3+}.

3.3 Field emission scanning electron microscopy (FEG-SEM).

Fig. 4(a) and (b) represents the FE-SEM images of the WO_3:Pr^{3+} particles obtained by the precipitation method. The chemical analysis with the elementary mapping of the WO_3:4% Pr^{3+} sample represented in Fig. 4(c) indicates the homogeneous distribution of the elements in the sample. It is observed that the predominant morphology of WO_3:Pr^{3+} are nanocubes with a well-dispersed particle size range. Check for the presence of irregularly shaped particles. It is possible to identify the presence of nanocubes formed completely by self-assembled nanoplates, as shown in the highlight of Fig. 4(a) and (b). This process of cubic particle formation is supported by the nucleation and growth stages, guaranteed by favorable conditions thermodynamically.

The particle size distribution was analyzed according to Fig. 4(a) and (b) using the LogNormal mathematical function as the fit curve, where X_c represents the average size of the analyzed particles. There is a variation in the average particle size as a function of the effect of the Pr^{3+} dopant. This effect can be justified by the charge compensation due to the replacement of W^{6+} ions by Pr^{3+} ions. This exchange leads to a load imbalance that can be counterbalanced by the creation of oxygen vacancy. This, in turn, induces a greater movement of the oxygen ion and, therefore, increases the growth of the crystals and the size of the particles. The favored stage, in this case, for the formation of the crystals is the growth stage. A similar behavior was observed by Mondal *et al.*[39] who related the effect of the $CaTiO_3$ particle size variation with various types of dopant and observed that according to the size of the doping cation there was a greater or lesser resistance to the formation of oxygen vacancy that was evidenced by the surface charge density present in the material.

The representative scheme of formation of the WO_3:Pr^{3+} nanocubes is illustrated in Fig. 5. Initially, the presence of precursor ions (W^{6+}/O^{2-}) dispersed in the reaction medium is observed under stirring and temperature conditions (60 °C). This phase is characterized by the nucleation step, with the formation of numerous WO_3 nuclei. In the next stage, there is the appearance of nanoplates from the aggregation of the nuclei. This process occurs in a random and spontaneous way until it reaches nanoplates of larger sizes.[40–42] The kinetics of crystal growth occur at the expense of smaller crystals that join larger crystals because they are more energetically stable, showing the stage of crystal growth. In the subsequent moment, these nanoplates acquire a certain degree of orientation in relation to each other. According to Moreira *et al.*[43] the increase in energy occurs during the self-assembly process of the nanoplates due to the disturbance of the structural lattice that is present in each nanoplate and as a result the elimination of the interface throughout the formation of the nanocubes. The final morphology obtained is cubic, constituted by the overlapping of nanoplanes.

Wang *et al.*[44] investigated the different crystal structure and morphological changes of WO_3 by the hydrothermal reaction as a function of changes in temperature and time of synthesis. WO_3 nanocubes are generated by the phase transition process

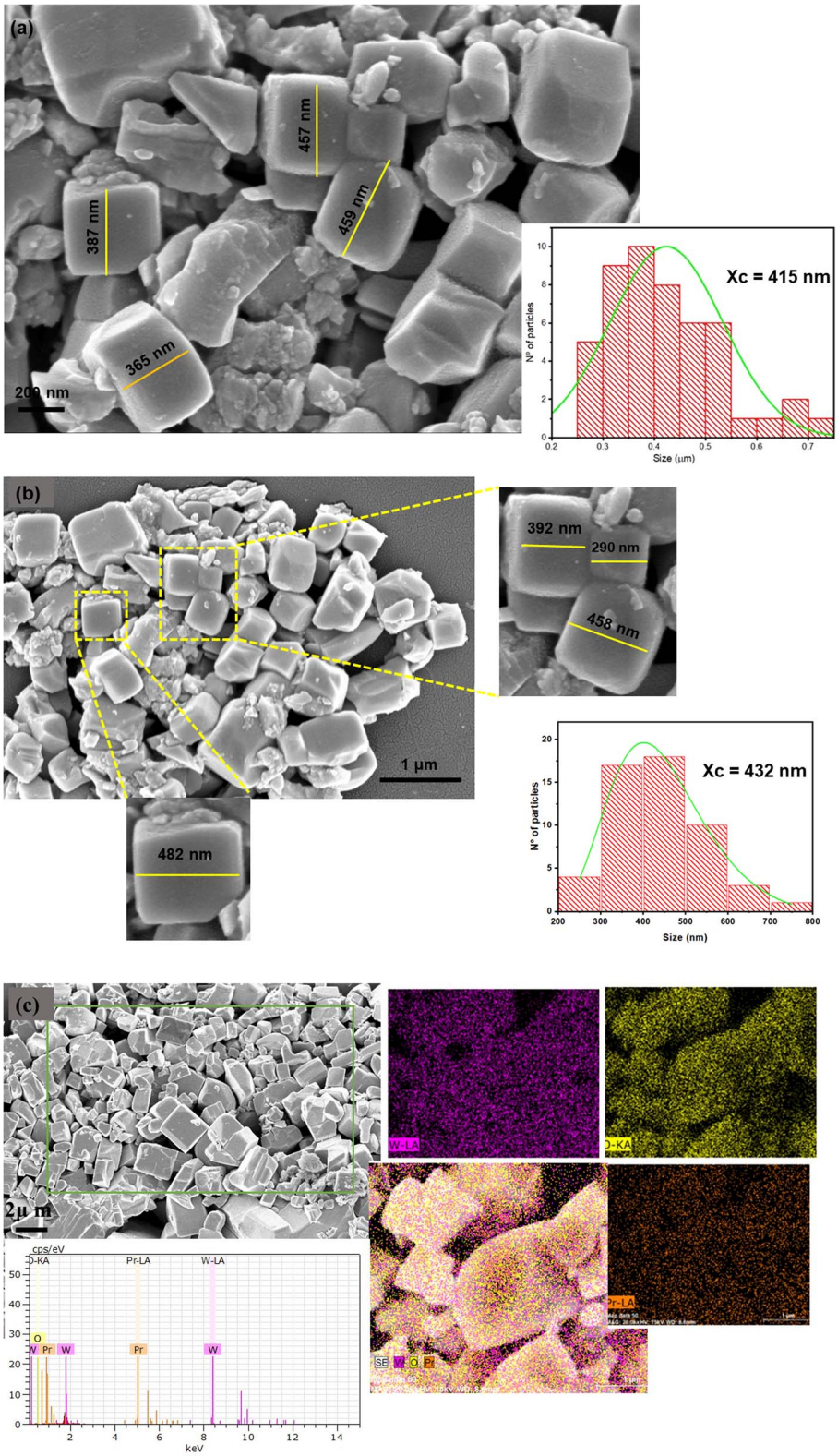

Fig. 4 SEM images and particle size distribution: (a) WO_3 sample; (b) WO_3:4%Pr^{3+} sample; (c) elementary mapping of WO_3:4%Pr^{3+} sample.

of the orthorhombic structure $WO_3 \cdot H_2O$, passing through another intermediate phase orthorhombic $WO_3 \cdot 0.33H_2O$ to monoclinic WO_3. In the initial stage, the formation of H_2WO_4 occurs when HNO_3 was added to the Na_2WO_4 aqueous solution. The structure of H_2WO_4 has layers of WO_6 octahedrons that share four equatorial oxygen atoms that are connected by

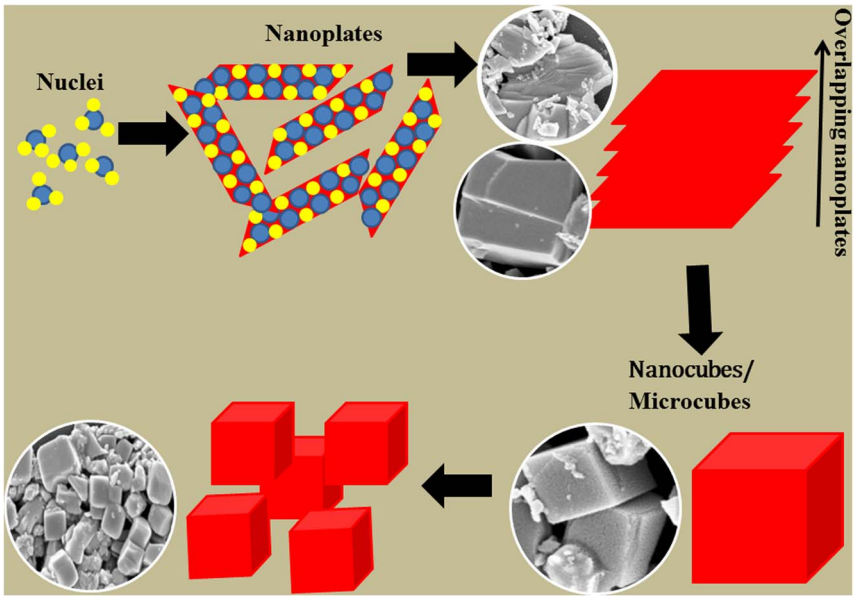

Fig. 5 Representative scheme of particle formation with nanocube morphology.

hydrogen bonds derived from the interaction between water molecules and the oxygen present in the axial position of the octahedron. The formation mechanism of WO_3 nanoparticles with growth direction depends on the solubility of metal oxides and the reaction kinetics during synthesis.

3.4 UV-vis spectroscopy

The optical properties of WO_3:Pr^{3+} particles were investigated from UV-Vis diffuse reflectance spectra as shown in Fig. 6(a). A broad optical absorption band is observed for the WO_3 sample in the visible region comprising the range from 430 to 800 nm. For samples doped with Pr^{3+}, a narrower asymmetric absorption band is observed with a maximum at 490 nm. This behavior is similar to that reported in other works,[45,46] which attributes this effect to the Plasmonic Resonance Surface. This behavior is related to the free electrons on the surfaces of metallic oxide particles, which results in a significant increase in the electrical conductivity of the material. The presence of oxygen vacancies in the material is a source of electron generation that participates in the plasmonic resonance effect.

The optical gap energy values (E_{gap}) were estimated from the Kubelka–Munk equation,[37,47] which is based on the transformation of diffuse reflectance measurements, to calculate E_{gap} measurements with acceptable precision. The Kubelka–Munk eqn (1) is described by:

$$\frac{K}{S} = \frac{(1-R)^2}{2R} = F(R) \quad (1)$$

where $F(R)$ is the Kubelka–Munk function or the absolute reflectance of the sample. In our case, barium sulfate (BaSO4) was adopted as the standard sample in the reflectance measurements, $R = R(\text{sample})/R(BaSO_4)$ (R is the reflectance), K is the molar absorption coefficient and S is the scattering coefficient. In a parabolic band structure, the optical band gap and the absorption coefficient of semiconductor oxides can be calculated by eqn (2):

$$\alpha h\nu = C(h\nu - E_{gap})^n \quad (2)$$

where α is the linear absorption coefficient of the material, $h\nu$ is the photon energy, C is a proportionality constant, E_{gap} is the optical band gap and n is a constant associated with different kinds of electronic transitions.

WO_3 presents an optical absorption spectrum governed by direct electronic transitions.[48,49] In this case, after electronic absorption, electrons located at least energy states in the conduction band (CB) are able to return for states of maximum energy of the valence band (VB), which is located in the same places in the Brillouin zone.

The estimated values for E_{gap} are within the range 2 and 2.65 eV. Change in E_{gap} values is observed for the doped samples due to the replacement of W^{6+} ions by Pr^{3+}. The optical gap is influenced by the dopant due to changes in densities of the localized electronic states. The XRD results show that the introduction of the dopant promoted an increase in peak intensity with a decrease in FWHM. This behavior signals an increase in the structural order and a decrease in localized states or defects, observing an increase in the size of the crystallite.

A. K. De *et al.*[50] followed an enlargement of the Ag_2O gap with Zn doping. According to the authors, a possible reason may be the presence of the doping atom orbitals in the VB or CB. This leads to hybridization with existing orbitals and results in changing energy levels. This conclusion was supported by the study of DOS graphics based on DFT calculations. According to Gonçalves *et al.*[51] the changes in the optical gap can be explained by the presence of the 4f orbitals of rare earth ions present in the microcrystalline lattice associated with new electronic levels in the band structure.

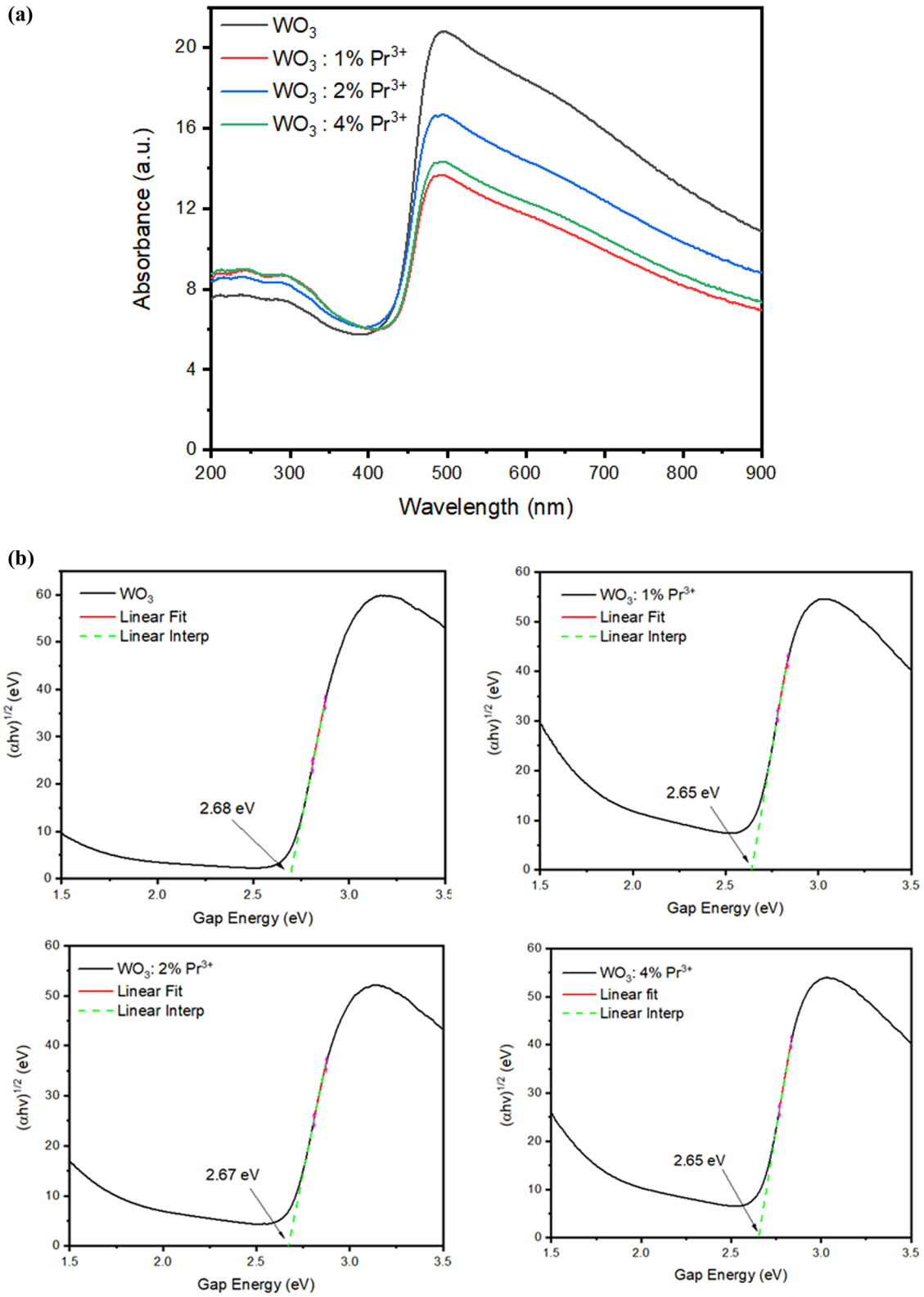

Fig. 6 (a) Absorption spectrum; (b) estimation of the gap energy (E_{gap}) by the Kubelka–Munk method.

3.5 Photoluminescence

Fig. 7(a) represents the photoluminescence spectra of samples WO_3 and WO_3:Pr^{3+} excited at a wavelength of 325 nm at room temperature. It is observed that the profile of the spectra has a broadband behavior that comprises the entire visible region. This feature is associated with the simultaneous contribution of several energy levels that radiatively decay from higher energy levels to lower energy levels within the WO_3 band gap, as occurs

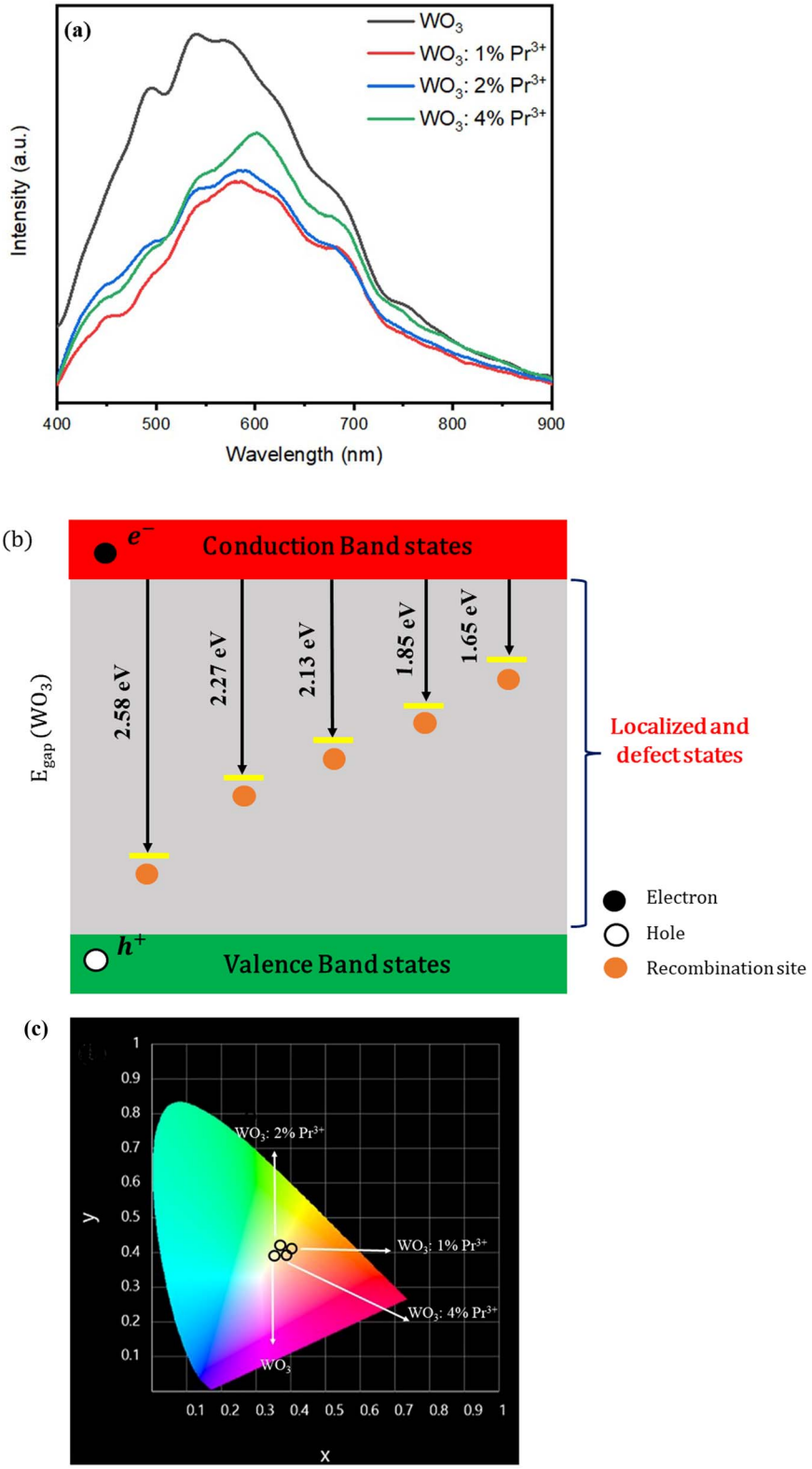

Fig. 7 (a) PL emission spectrum of WO_3 and WO_3:Pr^{3+} samples (λ_{exc} = 325 nm); (b) scheme the structure of energy bands (c) chromaticity diagram of samples WO_3 and WO_3:Pr^{3+}.

with other ceramic matrices.[52,53] The WO_3 sample has a higher photoluminescence intensity when compared to Pr^{3+} doped samples.

According to works reported in the literature, the origin of PL in WO_3 is a factor that stems from some conditions related to the presence of defects, such as: Frenkel defect, interstitial

defects, substitute chemical impurities, surface defects.[54,55] Photoluminescence is strongly sensitive to defects present on the surface, because the surface has abrupt changes in physical properties due to the large number of existing defects. The emission bands centered around 480, 545, 580, 670 and 750 nm are possibly attributed to localized states and levels of density defects in the band gap: acting as traps (recombination) for electron centers and holes.[56,57] It is observed that the emission band at 580 nm is shifted to 605 nm in samples doped with Pr^{3+}. The Fig. 7(b) based on the photoluminescence results; a scheme is proposed illustrating the structure of energy bands considering the recombination sites of electrons/holes within the band gap.

The presence of intermediate energy levels within the band gap spacing function as recombination sites for photogenerated charges in the excitation process. The increase in the rate of recombination of these charges favors the emission of photons. Thus, an increase in photoluminescent intensity is observed. Doping generates electronic defects within the ceramic matrix. As a strategy to neutralize the excess charges, other defects arise, such as oxygen vacancy, interstitial atoms. The narrowing of the band gap facilitates the transitions between electronic bands. On the other hand, when the rate of recombination of electrons/holes is very high, it causes a reduction in the production of oxidizing agents (O_2^- and $^{\bullet}OH^-$), so that the photocatalytic activity is compromised. In short, the photoluminescent and photocatalytic properties compete as a function of the rate of recombination of electrons and holes. However, other factors must be considered such as surface area, morphology, crystallinity of the particles.

Wang *et al.*[58] consider that PL emission is related to the band–band transition and the defect level transition. Second Wang *et al.*,[59] in another study regarding the effects of surfactant on the synthesis of WO_3 particles, classified into three types of oxygen vacancies in non-stoichiometric WO_3: neutral V_O^0, single charged V_O^+, and doubly charged V_O^{2+} states. In the electronic structure, the V_O^0 and V_O^{2+} states form the resonant state levels in the valence and conduction bands, and the V_O^+ state form a level in the bandgap.[60] Therefore, different transitions give rise to different PL emissions.

From the spectral distribution of the PL intensity, it was possible to calculate the photometric parameters and qualify the photoluminescent properties of the samples as recorded in Table 1. The chromaticity coordinates are presented in Fig. 7(c). It can be observed that all samples presented emission in the region of white. The chromaticity coordinates of WO_3 (0.35, 0.39) were closer to the ideal white color (0.33, 0.33). White emission is attributed to simultaneous emissions that occur throughout the entire visible spectrum in accordance with the broadband aspect shown in Fig. 7(a). It is reasonable to consider that there was an adjusted contribution of PL emission from the blue, green and red region, resulting in blank emission. A similar behavior is also verified in other works.[61,62] The samples showed a high color reproduction index, reaching a value of 90% for the WO_3:4%Pr^{3+} sample, which indicates a degree of reliability in the way colors are reproduced in a given light source.

Table 1 CIE coordinates and photometric data

Samples	WO_3	WO_3:1%Pr^{3+}	WO_3:2%Pr^{3+}	WO_3:4%Pr^{3+}
CIE (x, y)	(0.35, 0.39)	(0.39, 0.42)	(0.37, 0.39)	(0.39, 0.40)
CCT (K)	4821	4041	4173	3725
CRI (%)	87	85	87	90
Color	White	White	White	White
LER (lm W^{-1})	260	268	253	250

3.6 Photodegradation of crystal violet

Fig. 8 shows the degradation efficiency of the WO_3:x% Pr^{3+} powders against the crystal violet dye under UV light. The first 30 minutes of the test were carried out without radiation incidence so that the system reached the adsorption–desorption equilibrium.[63] After this time, the lights were turned on. It is possible to observe that less than 20% of the dye is removed in the photolysis process, while more than 60% of the dye is removed in the presence of WO_3:x% Pr^{3+} photocatalysts, highlighting the importance of using photocatalysts in the degradation of organic contaminants. Furthermore, the influence of doping is observed in the increase in degradation efficiency with increasing dopant content: while pure WO_3 powders degraded only 64% of the dye, WO_3:2%Pr^{3+} and WO_3:4%Pr^{3+} powders degraded 71.4% and 72.8%, respectively. Generally, rare earth metal ions can act either as a mediator of interfacial charge transfer or as a recombination center,[64] will depend on the amount of dopant used. Here, the improved photocatalytic efficiency for WO_3:2%Pr^{3+} and WO_3:4%Pr^{3+} powders is explained by the low PL intensity of these samples compared to pure WO_3, indicating that the introduction of Pr^{3+} promoted the increase in the efficiency of interfacial charge transfer, the decrease in the rate of recombination of the photogenerated e^-/h^+ pairs, consequently increasing the lifetime of the charge carriers.

The praseodymium dopant can exist as Pr^{3+} and Pr^{4+}. Thus, Pr^{3+} can donate an electron to O_2 adsorbed on the surface of the catalyst doped with Pr to form O_2^- (ref. 65) transforming into Pr^{4+}, favoring a charged migration to O_2 and increasing the photoreaction rate compared to the of pure WO_3.[64] Thus, Pr^{4+} can

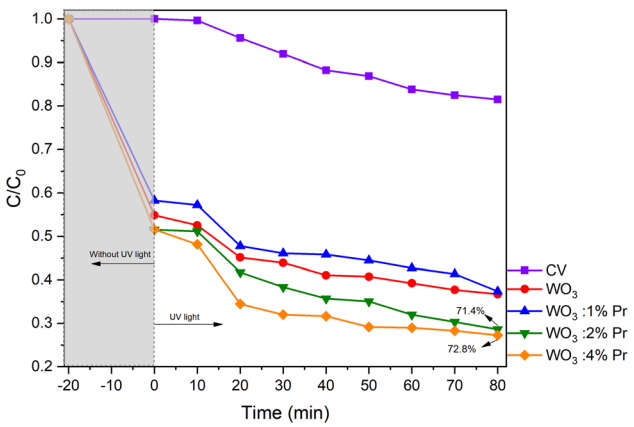

Fig. 8 Variation of CV concentration during its photocatalytic degradation by the action of WO_3:Pr^{3+} particles.

receive photogenerated electrons in the WO_3 conduction band to form Pr^{3+}, thus preventing the recombination of e^- with h^+.

The gap energy values for the WO_3 sample and for the series doped with Pr^{3+} showed very close values and in accordance with the results found in the literature,[66] with a subtle decrease when Pr^{3+} was incorporated into the WO_3 host matrix. The determination of the band gap value is an estimate that considers an average of the band gap of each face that constitutes the morphology of the particles. Each face has different characteristics, specificities in electronic density, surface defects (surface energy). These particularities allow promoting different responses in morphological aspects and surface properties: photocatalysis and photoluminescence. The measurement of the band gap value is related to the arrangement of the identified faces of each nanostructure.[67] It is observed according to Fig. 6(b) that the presence of Pr^{3+} did not significantly alter the band gap structure.

To understand the photocatalytic mechanism, 1 mmol of the reagents $AgNO_3$, EDTA, ascorbic acid (AA) and isopropyl alcohol (ISO) were used to capture the radicals e^-, h^+, O_2^- and $^{\bullet}OH^-$, respectively. It is observed in Fig. 9 that the addition of $AgNO_3$ did not influence the dye degradation efficiency. However, the addition of ISO, EDTA and AA compromised the degradation efficiency revealing that the main radicals in the degradation of the CV organic contaminant are the radicals $^{\bullet}OH^-$, h^+ and O_2^-, in that order.

From this, the possible degradation reactions are described below:

$$WO_3{:}x\%Pr + h\nu \rightarrow WO_3{:}x\%Pr + e^- + h^+$$

$$Pr^{3+} + O_2 \rightarrow O_2^- + Pr^{4+}$$

$$Pr^{4+} + e^- \rightarrow Pr^{3+}$$

$$h^+ + H_2O \rightarrow \dot{H} + O\dot{H}$$

$$O\dot{H} + h^+ + O_2^- + CV \rightarrow H_2O + CO_2 + \text{other inorganic molecules}$$

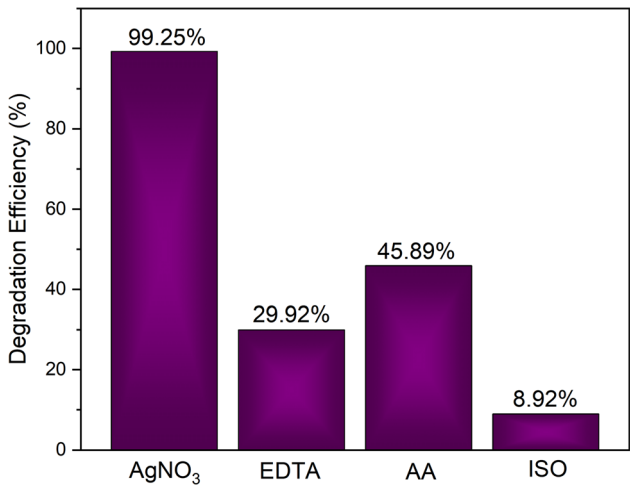

Fig. 9 Test with inhibitors for WO_3:4%Pr.

3.7 Correlation analysis between photoluminescent and photocatalytic properties

The WO_3 sample showed a higher photoluminescent intensity with a broad profile feature in the PL spectrum. This performance presented by WO_3 is in agreement with other studies in the literature.[66,68] It is reasonable to consider that the photon emission process is due to multiple relaxation processes with the participation of different energy levels. Associated with this behavior, it is possible to consider the existence of defects and structural distortions and their densities, which enable the formation of sites for trapping the e^-/h^+ charges, demanding an increase in the recombination rate and an increase in the intensity of photoluminescence.

The effect of Pr^{3+} ions on the WO_3 matrix did not effectively favor the increase in PL. Contrary, a decrease in the intensity of the photoluminescence is observed due to the decrease in the rate of recombination of the e^-/h^+ charges. This behavior does not occur linearly, which can be attributed to other factors such as the crystallinity of the material, surface properties (surface area) and morphological aspects: (i) average particle size, (ii) stability of crystallographic planes as a function of the evaluated properties (surface energy). This non-linear behavior is described by other authors,[69,70] who correlate the intensity of the photoluminescent property as a function of the particular density of electronic defects on the surfaces of the particles.

However, the photocatalytic activity was enhanced by the effect of Pr^{3+} ions. There is an increase in the photodegradation of the crystal violet dye for the sample with 4% Pr^{3+} compared to the sample without doping. A direct relation to this performance is attributed to the decrease in the rate of recombination of the photogenerated loads and, as a result, the increase in the production of oxidizing agents O_2^- and $^{\bullet}OH^-$ acting in the mineralization of organic molecules. Zheng *et al.*[70] confirm the positive effect of the selection of metal ions for doping the WO_3 structure with favorable results in the improvement of the photocatalytic activities.

4. Conclusion

The WO_3:Pr^{3+} particles were successfully prepared by the precipitation method followed by calcination. The introduction of Pr^{3+} promoted structural changes in the WO_3 metrics, inducing distortions such as: shortening of W–O bonds and changes in the growth kinetics of the particles. The formation of nanocubes was proposed by the superposition of several sheets of nanometric thickness resulting in the final morphology of the WO_3 particles. The photoluminescence spectra of WO_3 and WO_3:Pr^{3+} exhibited a broad band profile characteristic of the presence of surface defects in the particles. These defects functioned as a recombination center for the photogenerated charges. The increase in the concentration of Pr^{3+} ions promoted an increase in the intensity of photoluminescence. The WO_3 sample showed blank emission with CIE coordinates equal to (0.35, 0.39). Sample WO_3:4%Pr^{3+} exhibited a color reproducibility index of 90%. The best photocatalytic activity was obtained by the WO_3:2%Pr^{3+} and WO_3:4%Pr^{3+} samples, in

which both had PL intensity below pure WO_3 intensity, which indicates the low recombination of electron pairs e^-/h^+. The formation and participation of radicals $^{\bullet}OH$, h^+ and O_2^- in the degradation of organic dyes when WO_3 is used as a photocatalyst has been confirmed.

Compliance with ethical standards

The authors declare that they have no known competing financial interests or personal relationships that could have appeared to influence the work reported in this paper.

Data availability

All data generated or analysed during this study are included in this published article [and its ESI† files].

Author contributions

L. X. Lovisa: carried out the discussion of the results and the writing of the work; D. F. Dos Santos: performed the practical part to obtain the materials and carried out the photocatalytic tests and their analysis; A. A. G. Santiago: performed the structural refinement and the analysis of the results of the Rietveld refinements; M. D. Teodoro: carried out the photoluminescent measurements. M. R. D. Bomio: collaborated with carrying out the photocatalytic tests and writing the work; F. V. Motta: collaborated with the discussion of the results.

Conflicts of interest

There is no interest that directly and/or indirectly influences the work on the part of the authors that could compromise the appreciation of the work.

References

1 Z. Saddique, M. Imran, A. Javaid, S. Latif, T. H. Kim, M. Janczarek, M. Bilal and T. Jesionowski, Bio-fabricated bismuth-based materials for removal of emerging environmental contaminants from wastewater, *Environ. Res.*, 2023, **229**, 115861.

2 S. Ahmed, M. Mofijur, S. Nuzhat, A. T. Chowdhury, N. Rafa, M. A. Uddin, A. Inayat, T. Mahlia, H. C. Ong and W. Y. Chia, Recent developments in physical, biological, chemical, and hybrid treatment techniques for removing emerging contaminants from wastewater, *J. Hazard. Mater.*, 2021, **416**, 125912.

3 P. A. Shinde and S. C. Jun, Review on recent progress in the development of tungsten oxide based electrodes for electrochemical energy storage, *ChemSusChem*, 2020, **13**(1), 11–38.

4 N. V. Mdlovu, K.-S. Lin, C.-J. Chang, Y.-S. Lina and S. F. Hassan, Adsorption and photocatalytic degradation of dye contaminants in wastewater over W-doped titania nanotubes, *J. Taiwan Inst. Chem. Eng.*, 2023, **146**, 104863.

5 A. Nawaz, M. Atif, A. Khan, M. Siddique, N. Ali, F. Naz, M. Bilal, T. H. Kim, M. Momotko and H. U. Haq, Solar light driven degradation of textile dye contaminants for wastewater treatment–studies of novel polycationic selenide photocatalyst and process optimization by response surface methodology desirability factor, *Chemosphere*, 2023, **328**, 138476.

6 L. Bilińska and M. Gmurek, Novel trends in AOPs for textile wastewater treatment. Enhanced dye by-products removal by catalytic and synergistic actions, *Water Resour. Ind.*, 2021, **26**, 100160.

7 C. Dong, W. Fang, Q. Yi and J. Zhang, A comprehensive review on reactive oxygen species (ROS) in advanced oxidation processes (AOPs), *Chemosphere*, 2022, **308**, 136205.

8 C. B. Ong, L. Y. Ng and A. W. Mohammad, A review of ZnO nanoparticles as solar photocatalysts: Synthesis, mechanisms and applications, *Renewable Sustainable Energy Rev.*, 2018, **81**, 536–551.

9 A. A. P. Khan, P. Singh, P. Raizada and A. M. Asiri, Synthesis of magnetically separable $Bi_2O_2CO_3$/carbon nanotube/$ZnFe_2O_4$ as Z-scheme heterojunction with enhanced photocatalytic activity for water purification, *J. Sol-Gel Sci. Technol.*, 2020, **95**, 408–422.

10 Y. Fu and Q. Ma, Recent developments in electrochemiluminescence nanosensors for cancer diagnosis applications, *Nanoscale*, 2020, **12**(26), 13879–13898.

11 G. Singh, J. Lee, A. Karakoti, R. Bahadur, J. Yi, D. Zhao, K. AlBahily and A. Vinu, Emerging trends in porous materials for CO_2 capture and conversion, *Chem. Soc. Rev.*, 2020, **49**(13), 4360–4404.

12 A. J. Moreira, L. O. Campos, C. P. Maldi, J. A. Dias, E. C. Paris, T. R. Giraldi and G. P. Freschi, Photocatalytic degradation of Prozac® mediated by TiO_2 nanoparticles obtained via three synthesis methods: sonochemical, microwave hydrothermal, and polymeric precursor, *Environ. Sci. Pollut. Res.*, 2020, **27**, 27032–27047.

13 A. Gouasmia, E. Zouaoui, A. A. Mekkaoui, A. Haddad and D. Bousba, Highly efficient photocatalytic degradation of malachite green dye over copper oxide and copper cobaltite photocatalysts under solar or microwave irradiation, *Inorg. Chem. Commun.*, 2022, **145**, 110066.

14 D. F. Dos Santos, A. A. Santiago, M. D. Teodoro, F. V. Motta and M. R. Bomio, Investigation of the photocatalytic and optical properties of the $SrMoO_4$/g-C_3N_4 heterostructure obtained via sonochemical synthesis with temperature control, *J. Environ. Manage.*, 2023, **325**, 116396.

15 A. D. Gupta, H. Singh, S. Varjani, M. K. Awasthi, B. S. Giri and A. Pandey, A critical review on biochar-based catalysts for the abatement of toxic pollutants from water via advanced oxidation processes (AOPs), *Sci. Total Environ.*, 2022, **849**, 157831.

16 Z. H. Jabbar and S. E. Ebrahim, Recent advances in nano-semiconductors photocatalysis for degrading organic contaminants and microbial disinfection in wastewater: A comprehensive review, *Environ. Nanotechnol., Monit. Manage.*, 2022, **17**, 100666.

17 C. Vanitha, R. Abirami, S. Chandraleka, M. Kuppusamy and T. Sridhar, Green synthesis of photocatalyst hydroxyapatite doped TiO_2/GO ternary nanocomposites for removal of methylene blue dye, *Mater. Today: Proc.*, 2023, DOI: 10.1016/j.matpr.2023.02.354.
18 K. Bhavsar, P. Labhane, V. Huse, R. Dhake and G. Sonawane, Activated carbon immobilized WO_3 nanocuboids: Adsorption/photocatalysis synergy for the enhanced removal of organic pollutants, *Inorg. Chem. Commun.*, 2020, **121**, 108215.
19 L. Zhao, X. Xi, Y. Liu, L. Ma and Z. Nie, Growth mechanism and visible-light-driven photocatalysis of organic solvent dependent WO3 and nonstoichiometric WO3-x nanostructures, *J. Taiwan Inst. Chem. Eng.*, 2020, **115**, 339–347.
20 N. Shaheen, M. F. Warsi, S. Zulfiqar, J. T. Althakafy, A. K. Alanazi, M. I. Din, H. M. Abo-Dief and M. Shahid, La-doped WO3@ gCN Nanocomposite for Efficient degradation of cationic dyes, *Ceram. Int.*, 2023, **49**, 15507–15526.
21 M. M. Rhaman, S. Ganguli, S. Bera, S. B. Rawal and A. K. Chakraborty, Visible-light responsive novel WO3/TiO2 and Au loaded WO3/TiO2 nanocomposite and wastewater remediation: mechanistic inside and photocatalysis pathway, *J. Water Process Eng.*, 2020, **36**, 101256.
22 R. Rong and L. Wang, Synthesis of hierarchical hollow nest-like WO3 micro/nanostructures with enhanced visible light-driven photocatalytic activity, *J. Alloys Compd.*, 2021, **850**, 156742.
23 S. P. Gupta, H. Nishad, V. Magdum and P. S. Walke, High-performance supercapacitor electrode and photocatalytic dye degradation of mixed-phase WO3 nanoplates, *Mater. Lett.*, 2020, **281**, 128639.
24 V. Saasa and B. Mwakikunga, Facile Synthesis, Characterization and Acetone Sensing Properties of n-type WO3, SnO2 and VO2 Semiconducting Materials and their cobalt doped performance: Outstanding SnO2-Co Acetone Selectivity and Sensitivity, *Mater. Res. Bull.*, 2023, 112288.
25 B. Zhang, J. Luo, Z. Chen, L. Wu, J. Li, Y. Tian and S. Liu, Synthesis, characterization and dual-band electrochromic properties of Nb-doped WO3 films, *J. Electroanal. Chem.*, 2022, **918**, 116487.
26 Q. Zheng and C. Lee, Visible light photoelectrocatalytic degradation of methyl orange using anodized nanoporous WO3, *Electrochim. Acta*, 2014, **115**, 140–145.
27 A. Haroon and A. S. Ahmed, An insight into the microstructural properties and dielectric behavior of Ce doped WO3 nanoparticles, *Phys. B*, 2023, **657**, 414798.
28 S. B. Upadhyay, R. K. Mishra and P. P. Sahay, Structural and alcohol response characteristics of Sn-doped WO3 nanosheets, *Sens. Actuators, B*, 2014, **193**, 19–27.
29 B. D. Cullity, *Elements of X-ray Diffraction*, Addison-Wesley Publishing, 1956.
30 F. Wang, C. Di Valentin and G. Pacchioni, Semiconductor-to-metal transition in WO 3− x: Nature of the oxygen vacancy, *Phys. Rev. B: Condens. Matter Mater. Phys.*, 2011, **84**(7), 073103.
31 R. Chatten, A. V. Chadwick, A. Rougier and P. J. Lindan, The oxygen vacancy in crystal phases of WO3, *J. Phys. Chem. B*, 2005, **109**(8), 3146–3156.
32 M. B. Johansson, G. Baldissera, I. Valyukh, C. Persson, H. Arwin, G. A. Niklasson and L. Österlund, Electronic and optical properties of nanocrystalline WO3 thin films studied by optical spectroscopy and density functional calculations, *J. Phys.: Condens. Matter*, 2013, **25**(20), 205502.
33 B. Chen, J. Laverock, L. Piper, A. Preston, S. Cho, A. DeMasi, K. Smith, D. Scanlon, G. Watson and R. Egdell, The band structure of WO3 and non-rigid-band behaviour in Na0. 67WO3 derived from soft x-ray spectroscopy and density functional theory, *J. Phys.: Condens. Matter*, 2013, **25**(16), 165501.
34 P. Woodward, A. Sleight and T. Vogt, Structure refinement of triclinic tungsten trioxide, *J. Phys. Chem. Solids*, 1995, **56**(10), 1305–1315.
35 G. M. Kumar, D. Lee, H. Jeon, P. Ilanchezhiyan, K. D. Young and K. T. Won, One dimensional ZnWO4 nanorods coupled with WO3 nanoplates heterojunction composite for efficient photocatalytic and photoelectrochemical activity, *Ceram. Int.*, 2022, **48**(3), 4332–4340.
36 S. Tripathi, D. Tripathi, R. K. Rawat and P. Chauhan, Room temperature operable solid-state sensors for selective methanol vapour detection from orthorhombic WO_3 nanoplates, *Mater. Lett.*, 2023, 133840.
37 D. Li, Y. Liu, Y. Yang, G. Tang and H. Tang, Rational construction of Ag3PO4/WO3 step-scheme heterojunction for enhanced solar-driven photocatalytic performance of O2 evolution and pollutant degradation, *J. Colloid Interface Sci.*, 2022, **608**, 2549–2559.
38 S. Chen, Y. Xiao, W. Xie, Y. Wang, Z. Hu, W. Zhang and H. Zhao, Facile strategy for synthesizing non-stoichiometric monoclinic structured tungsten trioxide (WO_{3-x}) with plasma resonance absorption and enhanced photocatalytic activity, *Nanomaterials*, 2018, **8**(7), 553.
39 O. Mondal, M. Pal, R. Singh, D. Sen and S. Mazumder, Influence of doping on crystal growth, structure and optical properties of nanocrystalline CaTiO3: a case study using small-angle neutron scattering, *J. Appl. Crystallogr.*, 2015, **48**(3), 836–843.
40 M. L. Moreira, E. C. Paris, G. S. do Nascimento, V. M. Longo, J. R. Sambrano, V. R. Mastelaro, M. I. Bernardi, J. Andrés, J. A. Varela and E. Longo, Structural and optical properties of CaTiO3 perovskite-based materials obtained by microwave-assisted hydrothermal synthesis: An experimental and theoretical insight, *Acta Mater.*, 2009, **57**(17), 5174–5185.
41 V. Longo, A. De Figueiredo, S. De Lázaro, M. Gurgel, M. Costa, C. Paiva-Santos, J. A. Varela, E. Longo, V. R. Mastelaro and F. De Vicente, Structural conditions that leads to photoluminescence emission in Sr Ti O 3: An experimental and theoretical approach, *J. Appl. Phys.*, 2008, **104**(2), 023515.
42 D. P. Volanti, I. L. Rosa, E. C. Paris, C. A. Paskocimas, P. S. Pizani, J. A. Varela and E. Longo, The role of the Eu3+

ions in structure and photoluminescence properties of SrBi2Nb2O9 powders, *Opt. Mater.*, 2009, **31**(6), 995–999.

43 M. L. Moreira, J. R. Bordin, J. Andrés, J. A. Varela and E. Longo, A description of the formation and growth processes of CaTiO 3 mesocrystals: a joint experimental and theoretical approach, *Mol. Syst. Des. Eng.*, 2020, **5**(7), 1255–1266.

44 L. Wang, H. Hu, J. Xu, S. Zhu, A. Ding and C. Deng, WO3 nanocubes: Hydrothermal synthesis, growth mechanism, and photocatalytic performance, *J. Mater. Res.*, 2019, **34**(17), 2955–2963.

45 H. Tang, Z. Tang, J. Bright, B. Liu, X. Wang, G. Meng and N. Wu, Visible-Light Localized Surface Plasmon Resonance of WO3−x Nanosheets and Its Photocatalysis Driven by Plasmonic Hot Carriers, *ACS Sustainable Chem. Eng.*, 2021, **9**, 1500–1506.

46 K. Manthiram and A. Paul Alivisatos, Tunable Localized Surface Plasmon Resonances in Tungsten Oxide Nanocrystals, *J. Am. Chem. Soc.*, 2012, **134**, 3995–3998.

47 M. L. Myrick, M. N. Simcock, M. Baranowski, H. Brooke, S. L. Morgan and J. N. McCutcheon, The Kubelka-Munk diffuse reflectance formula revisited, *Appl. Spectrosc. Rev.*, 2011, **46**(2), 140–165.

48 N. Liu, R. Li, J. Zhu, Q. Liu, R. Chen, J. Yu, Y. Li, H. Zhang and J. Wang, Z-scheme heterojunction ZnS/WO3 composite: Photocatalytic reduction of uranium and band gap regulation mechanism, *J. Colloid Interface Sci.*, 2023, **630**, 727–737.

49 A. Shirpay and M. B. Mohagheghi, Dependence of structure and energy band gap on sensing properties of WO3: TeO2 thin films deposited by spray pyrolysis, *Phys. B*, 2022, **627**, 413615.

50 A. K. De, S. Majumdar, S. Pal, S. Kumar and I. Sinha, Zn doping induced band gap widening of Ag2O nanoparticles, *J. Alloys Compd.*, 2020, **832**, 154127.

51 R. Gonçalves, L. Cavalcante, I. Nogueira, E. Longo, M. Godinho, J. Sczancoski, V. R. Mastelaro, I. Pinatti, I. Rosa and A. Marques, Rietveld refinement, cluster modelling, growth mechanism and photoluminescence properties of CaWO 4: Eu 3+ microcrystals, *CrystEngComm*, 2015, **17**(7), 1654–1666.

52 M. C. Oliveira, J. Andres, L. Gracia, M. S. M. de Oliveira, J. M. R. Mercury, E. Longo and I. C. Nogueira, Geometry, electronic structure, morphology, and photoluminescence emissions of BaW1-xMoxO4 (x= 0, 0.25, 0.50, 0.75, and 1) solid solutions: Theory and experiment in concert, *Appl. Surf. Sci.*, 2019, **463**, 907–917.

53 L. Lovisa, D. Dos Santos, A. Santiago, M. Siu Li, E. Longo, F. Motta and M. Bomio, Enhanced red emission in Sr (1-x) EuxMo0. 5W0. 5O4 (x= 0.01, 0.02, 0.04) phosphor and spectroscopic analysis for display applications, *J. Mater. Sci.*, 2022, **57**(19), 8634–8647.

54 B. Wang, X. Zhong, J. Zhu, Y. Zhang, U. Cvelbar and K. Ostrikov, Single-step synthesis of sub-stoichiometric tungsten oxide particles in mixed acetic and oleic acids: Structural conversion and photoluminescence enhancement, *J. Alloys Compd.*, 2022, **899**, 163265.

55 T. Thongtem, S. Kungwankunakorn, B. Kuntalue, A. Phuruangrat and S. Thongtem, Luminescence and absorbance of highly crystalline CaMoO4, SrMoO4, CaWO4 and SrWO4 nanoparticles synthesized by co-precipitation method at room temperature, *J. Alloys Compd.*, 2010, **506**(1), 475–481.

56 Y. Zhydachevskyy, *et al.*, Band Gap Engineering and Trap Depths of Intrinsic Point Defects in $RAlO_3$ (R = Y, La, Gd, Yb, Lu) Perovskites, *J. Phys. Chem. C*, 2021, **125**, 26698–26710.

57 T. Leijtens, *et al.*, Carrier trapping and recombination: the role of defect physics in enhancing the open circuit voltage of metal halide perovskite solar cells, *Energy Environ. Sci.*, 2016, **9**, 3472–3481.

58 B. Wang, X. Zhong, C. He, B. Zhang, U. Cvelbar and K. Ostrikov, Nanostructure conversion and enhanced photoluminescence of vacancy engineered substoichiometric tungsten oxide nanomaterials, *Mater. Chem. Phys.*, 2021, **262**, 124311.

59 B. Wang, X. Zhong, H. Xu, Y. Zhang, U. Cvelbar and K. Ostrikov, Structure and Photoluminescence of WO3-x Aggregates Tuned by Surfactants, *Micromachines*, 2022, **13**(12), 2075.

60 S. K. Deb, Opportunities and challenges in science and technology of WO3 for electrochromic and related applications, *Sol. Energy Mater. Sol. Cells*, 2008, **92**(2), 245–258.

61 L. X. Lovisa, V. D. Araújo, R. L. Tranquilin, E. Longo, M. S. Li, C. A. Paskocimas, M. Bomio and F. V. d. Motta, White photoluminescence emission from ZrO2 co-doped with Eu3+, Tb3+ and Tm3+, *J. Alloys Compd.*, 2016, **674**, 245–251.

62 L. Lovisa, A. Santiago, M. Farias, B. Barros, E. Longo, M. S. Li, C. Paskocimas, M. Bomio and F. Motta, White light emission from single-phase Y2MoO6: xPr3+ (x= 1, 2, 3 and 4 mol%) phosphor, *J. Alloys Compd.*, 2018, **769**, 420–429.

63 K. Anwar, F. K. Naqvi, S. Beg and S. Haneef, Photocatalytic degradation of MB dye and paracetamol drug, via hydrothermally synthesised praseodymium doped Bi4V2O11 nanoparticles, *J. Mol. Struct.*, 2023, **1272**, 134183.

64 Y. Hanifehpour, B. Soltani, A. R. Amani-Ghadim, B. Hedayati, B. Khomami and S. W. Joo, Praseodymium-doped ZnS nanomaterials: Hydrothermal synthesis and characterization with enhanced visible light photocatalytic activity, *J. Ind. Eng. Chem.*, 2016, **34**, 41–50.

65 S. Athira, A. John and S. Solomon, Photocatalytic and thermodynamic study of Pr doped SrO nanoparticles, *Chem. Phys. Lett.*, 2022, **809**, 140162.

66 H. Widiyandari, I. Firdaus, V. G. S. Kadarisman and A. Purwanto, Optical Properties and Photocatalytic Activities of Tungsten Oxide (WO_3) with Platinum Co-Catalyst Addition, *AIP Conf. Proc.*, 2016, **1712**, 050027.

67 P. P. Ortega, R. A. C. Amoresi, M. D. Teodoro, E. Longo, M. A. Ponce and A. Z. Simões, Relationship among morphology, photoluminescence emission, and photocatalytic activity of Eu-doped ceria nanostructures: A surface-type effect, *Ceram. Int.*, 2023, **49**, 21411–21421.

68 F. Mehmood, J. Iqbal, T. Jan and Q. Mansoor, Structural, Raman and photoluminescence properties of Fe doped WO_3 nanoplates with anti cancer and visible light driven photocatalytic activities, *J. Alloys Compd.*, 2017, **728**, 1329–1337.

69 C. S. Prajapati, A. Kushwaha and P. P. Sahay, Influence of Fe doping on the structural, optical and acetone sensing properties of sprayed ZnO thin films, *Mater. Res. Bull.*, 2013, **48**, 2687.

70 F. Zheng, M. Guo and M. Zhang, Hydrothermal preparation and optical properties of orientation controlled WO_3 nanorod arrays on ITO substrates, *CrystEngComm*, 2013, **15**, 277.